NANO · MICRO small
www.small-journal.com

The Control of Colloidal Grain Boundaries through Evaporative Vertical Self-Assembly

*Youngjoon Suh, Quang Pham, Bowen Shao, and Yoonjin Won**

Self-assembly continuously gains attention as an excellent method to create novel nanoscale structures with a wide range of applications in photonics, optoelectronics, biomedical engineering, and heat transfer applications. However, self-assembly is governed by a diversity of complex interparticle forces that cause fabricating defectless large scale (>1 cm) colloidal crystals, or opals, to be a daunting challenge. Despite numerous efforts to find an optimal method that offers the perfect colloidal crystal by minimizing defects, it has been difficult to provide physical interpretations that govern the development of defects such as grain boundaries. This study reports the control over grain domains and intentional defect characteristics that develop during evaporative vertical deposition. The degree of particle crystallinity and evaporation conditions is shown to govern the grain domain characteristics, such as shapes and sizes. In particular, the grains fabricated with 300 and 600 nm sphere diameters can be tuned into single-column structures exceeding ≈1 mm by elevating heating temperature up to 93 °C. The understanding of self-assembly physics presented in this work will enable the fabrication of novel self-assembled structures with high periodicity and offer fundamental groundworks for developing large-scale crack-free structures.

1. Introduction

Modern nanoscale fabrication techniques such as self-assembly nanofabrication have been utilized to design and construct novel material architectures with unprecedented levels of control over structural properties.[1–3] Self-assembly is a fundamental phenomenon where the components of a system assemble themselves to form a structural organization.[4,5] The driving force of self-assembly can typically be attributed to interparticle interactions that are governed by preferential thermodynamic states, in which particles seek open lattice sites to minimize the local free energy of the system. Therefore, the boundary conditions of the thermodynamic equilibrium process can play a sensitive role in affecting the self-assembly process, leading to various by-products of self-assembly.[6,7]

The self-assembly of monodispersed spheres to form colloidal crystals, often referred to as opals, can occur through various methods, such as spin-coating,[8] Langmuir–Blodgett,[9] gravity sedimentation,[10] or vertical deposition,[11,12] which all leverage capillary-driven self-assembly of spherical particles. Spin-coating enables rapid self-assembly but produces poor crystalline packing in the radial direction. Langmuir–Blodgett provides structural regularity but is difficult to create thicker opal films due to the extremely time-consuming process. Gravity sedimentation through drop-casting methods accommodates a wide variety of sphere diameters and can be easily implemented on the large scale. Unfortunately, drop-casting often produces unrepeatable and uncontrollable opal film features, such as arbitrary polycrystallinity and nonuniform structural thickness over the sample.[13]

As an alternative method, colloidal self-assembly through capillary-assisted evaporative vertical deposition receives significant attention because of its simplicity, well-controlled parameters, and its capability to fabricate highly crystalline packed structures.[9,11,14,15] The evaporative vertical deposition process (**Figure 1**a) relies on a hydrophilic substrate being vertically submerged in a colloidal suspension. The attractive capillary forces occurring near the thin film substrate–liquid meniscus cause the spheres to self-assemble into crystalline packing (Figure 1b). While the vertical deposition produces high-quality opaline structures, the process is relatively slow compared to spin-coating or drop-casting methods and is regarded as strongly dependent on the solvent's evaporation rate. Moreover, the fabrication of large-scale samples still remains challenging despite previous efforts.[16–18] Although the self-assembled sphere packing possesses a well-ordered crystalline arrangement at the microscale (<100 μm), it is difficult to observe perfect colloidal crystals at the macroscale (>100 μm) due to the creation of uncontrolled structural defects as a by-product of the self-assembly process (Figure 1c,d).[19,20] The formation of these defects creates undesirable structural properties for the colloidal crystal film, such as anisotropy in diffraction patterns and hydraulic resistances.[21–24]

The prominent contributors to defect formation during self-assembly can be identified into two categories: 1) First, particle defects, such as colloidal polydispersity, particle shapes, and impurities, affect the overall opal quality.[25,26] These types of defects increase the randomness of the structures and can be reduced by improving the manufacturing process of the spheres. 2) Second, structural defects that are generated by

Y. Suh, Q. Pham, B. Shao, Prof. Y. Won
Department of Mechanical and Aerospace Engineering
University of California
5200 Engineering Hall Irvine, Irvine, CA 92697–2700, USA
E-mail: won@uci.edu

The ORCID identification number(s) for the author(s) of this article can be found under https://doi.org/10.1002/smll.201804523.

DOI: 10.1002/smll.201804523

© 2019 WILEY-VCH Verlag GmbH & Co. KGaA, Weinheim

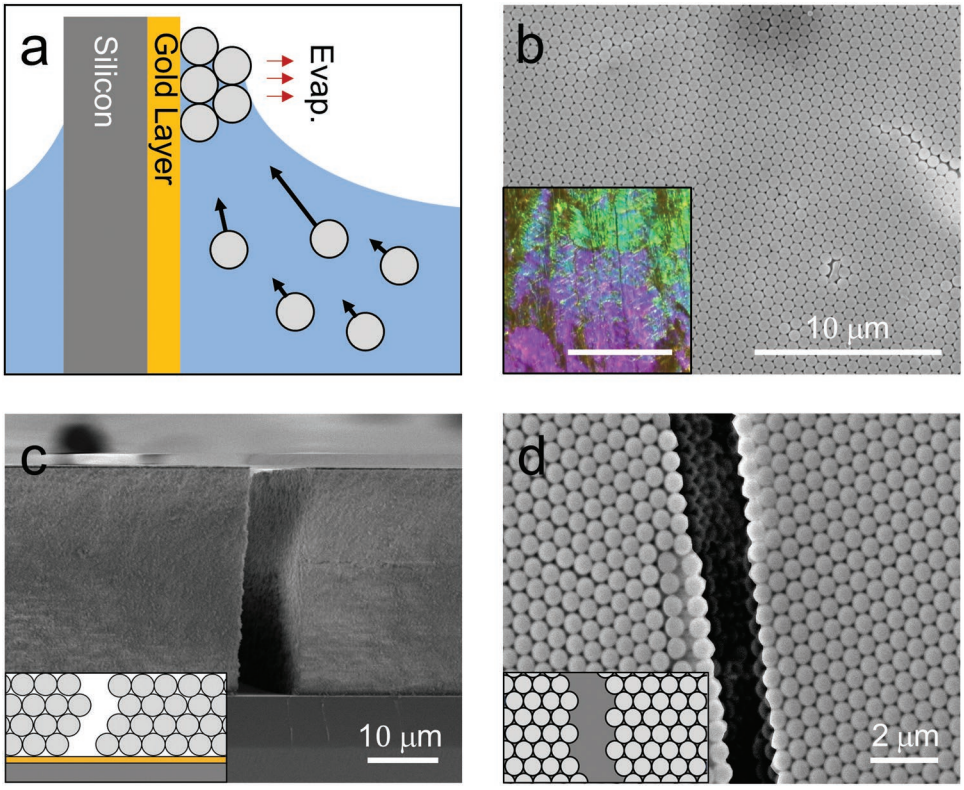

Figure 1. Colloidal self-assembly and polycrystalline opal characteristics. a) The schematic illustrates the general process of the vertical deposition method. A substrate with a gold pattern is vertically placed into a well of colloidal suspension that is heated at the base to promote gentle convective mixing and prevent sphere sedimentation. As the solvent evaporates, a thin film opal deposits at the substrate–liquid meniscus contact region due to water flows generated at the meniscus of the opal packing. b) The self-assembled opals exhibit crystallinity as confirmed by the scanning electron microscope (SEM) image and optical light diffraction image (inset). c) Cross-sectional and d) top view SEM images and inset illustrations show the separation of crystalline opal grains by microcracks denoted as grain boundaries.

local packing types impact the overall opal packing quality as well.[27,28] During self-assembly, the spheres assemble themselves to form simple structures (i.e., body-centered cubic (BCC), face-centered cubic (FCC), and hexagonal close-packed (HCP)) to minimize the local free energy of the system. Although the FCC packing is theoretically the most thermodynamically stable,[28] and thus the most favorable structure,[5] the small energy differences between the BCC, FCC, and HCP packings engender mixed packing phases within the crystalline structure, which generates packing misalignment and vacancies, ultimately contributing to the formation of cracks.[21,29] These microcracks are a common type of structural defects produced in multilayered opals when tensile forces generated from the evaporating liquid menisci between the self-assembling spheres overcome the interparticle attractive forces.[20] As a result, individual colloidal crystal domains or "grains" are separated by distinct microcracks, which are denoted as "grain boundaries."[20] The mechanistic formation of grain boundaries has been controllable by modulating process parameters (e.g., particle size, temperature, colloidal concentration, and humidity) related to the evaporation rates of the colloidal solution.[13,18,30,31]

There have been numerous efforts to investigate the crack formation physics in relation to the process parameters, with the aim of minimizing defects.[19,32,33] For example, higher evaporation temperatures lead to larger capillary-liquid flows toward the packed spheres, which increase the kinetic energy of the colloids and allow them to explore favorable lattice sites,[13,18,30,31] resulting in a decrease in defect density.[13] Furthermore, previous studies have proposed the theoretical possibility of creating crack-free structures by maintaining the structural thickness under a certain value, known as the critical thickness.[20,34] The structural thickness, in turn, is determined by the balance between colloidal concentration and sphere diameter.[26,30] The majority of these studies that examine colloidal self-assembly can be divided into two major thrusts: 1) The first thrust proposes various recipes to create opal films with high crystalline quality and minimum defects.[13,18,19,27,35] In these processes, fundamental backgrounds have been established based on how different experimental parameters affect the vertical deposition process. Despite numerous efforts to fabricate perfect large-scale colloidal crystals, it has been impossible to eliminate structural defects entirely. 2) The second thrust leverages the existence of these defects to develop unique patterned structures and utilize them for potential applications (i.e., transparent conductive films, microfluidics, and sensor arrays).[36–38] However, many of these studies often underexplore the underlying physics of these defects, which can cause the samples to be difficult to replicate in different conditions.

© 2019 WILEY-VCH Verlag GmbH & Co. KGaA, Weinheim

In this study, we control the propagation and development of structural defects in colloidal crystals produced during the evaporative vertical deposition self-assembly of polystyrene spheres. A new image processing technique presented here quantitively measures the sphere packing quality while it simultaneously identifies defect types, such as impurities, vacancies, and misalignments. Furthermore, the combination of evaporative conditions is modulated by varying the sphere diameter (100–600 nm), colloidal concentration, and heating temperature, in order to investigate their effects on grain characteristics (i.e., grain domains and boundaries). Additionally, computational simulation models are developed to calculate evaporative parameters (i.e., evaporative mass flux, heat transfer coefficient, and domain drying time) at the liquid–vapor interfaces in the opal packing and microcrack domains. The combined efforts of experimental and numerical work identify the mechanisms for controlling crack propagation and grain development via self-assembly, which may be used to create periodically arranged, porous nanostructures with well-defined grain features or to develop large-scale, crack-free structures. Therefore, the insights from this study can promise performance breakthroughs for applications that require precise design of optical properties,[24,39–41] fluid transport characteristics,[42–46] and mechanical functionality.[47–50]

2. Results and Discussion

2.1. Crack Initiation and Development

We investigate the vertical deposition self-assembly process by systematically applying different combinations of sphere diameter, colloidal concentration, and heating temperature to modulate crack and grain characteristics. During the fabrication process, the typical opal film is subcategorized into three regimes depending on the liquid–solid saturation levels during vertical deposition: the dry, the wet, and the saturated regimes, as shown in **Figure 2**a. The dry regime is a region in which the self-assembled opal is completely dried with a dry length L_D. The wet regime is an intermediate region between dry and saturated with a wet length L_w. The saturated regime represents the colloidal solution domain and decreases over time, as the solution evaporates. The three regimes can be visually identified by the color differences within the sample.

As the solvent evaporates, the concentration of the solution changes with time, resulting in location-dependent grain[6,21,27] characteristics in terms of shapes and sizes. The location-dependent grains are subcategorized into three regimes that can be identified by noticing sudden changes in grain patterns: 1) the top regime, where the grain sizes are the smallest among all regimes, 2) the middle regime, where grains are noticeably stable in shape and size, and 3) the bottom regime, where grain size variations occur due to abrupt concentration differences. The coverage of each regime presented in Figure S1 (Supporting Information) for different sphere diameters shows that the middle regime constitutes ≈64–77% of the sample. The middle of the middle regime is selected as the area of interest in this study to reduce potential inconsistencies caused by location-dependent grain characteristics. More detailed information is provided in Supporting Information S1.

We investigate the initiation and propagation of cracks as well as the evolution of grains by utilizing real-time imaging techniques and numerical simulations. Crack initiation creates a gap between opal packings and emerges in forms of "crack seeds," as illustrated in Figure 2b. The crack seeds are produced due to tensile forces caused by evaporation-induced negative capillary pressures occurring at the meniscus of the opal packing,[20,51,52] and by individual sphere shrinkage upon drying.[1,53] As a relatively thick liquid film fills the gaps generated by the crack seeds, an evaporation rate misbalance between the opal packing domain and the crack domain occurs (Figure 2c).

We calculate the evaporation rates of both the opal packing domain and the crack domain by conducting numerical simulations for varying spherical diameters ranging from 0.1 to 100 μm (Supporting Information S2). In this numerical simulation, the evaporative mass flux (i.e., the rate that mass is leaving or entering the liquid–vapor interface) is calculated based on the liquid–vapor interface temperature, revealing that the evaporative mass flux increases as the sphere diameter decreases (Figure S3a,b, Supporting Information). The evaporative mass flux is used to compute the heat transfer coefficient (Figure S3c, Supporting Information) using Equation (S11) (Supporting Information), which is then used to calculate the domain drying time (i.e., time to completely evaporate liquid) using Equations (S12) and (S13) (Supporting Information). The plot in Figure S3d (Supporting Information) compares the drying time between the opal packing domain and the crack domain for varying liquid filling heights. This comparison reveals that the opal packing domain dries ≈10 times faster than the crack domain when the liquid filling height is ≈15 μm and the sphere diameter is 100 nm.

The drying time differences between the opal packing domain and the crack domain facilitate transverse (i.e., perpendicular to the drying direction) as well as longitudinal (i.e., parallel to the drying direction) crack propagations. While both crack types are governed by the same mechanisms, the longitudinal crack propagation is prominent due to the drying direction, and thereby propagates deep (≈600 μm) into the wet regime. By contrast, transverse cracks appear at a later stage, near the interface of the dry and wet regimes or within the dry regime close to the interface (Figure 2d,e). As a pair of both longitudinal (Figure 2c) and transverse cracks (Figure 2f) connect, they create an isolated opal domain (i.e., grain). The details of time evolution of crack formation are illustrated in Figure S4 (Supporting Information).

2.2. Crystalline Packing Quality

To understand the microcrack characteristics, it is imperative to identify the quality or "crystallinity" of the sphere packing. In the majority of past studies, opal crystallinity has been assessed by means of conventional transmittance tests.[13,19,35] These tests are useful in determining an integrative assessment of the film packing quality but cannot identify specific details of defect types. In this study, we present a rigorous determination

© 2019 WILEY-VCH Verlag GmbH & Co. KGaA, Weinheim

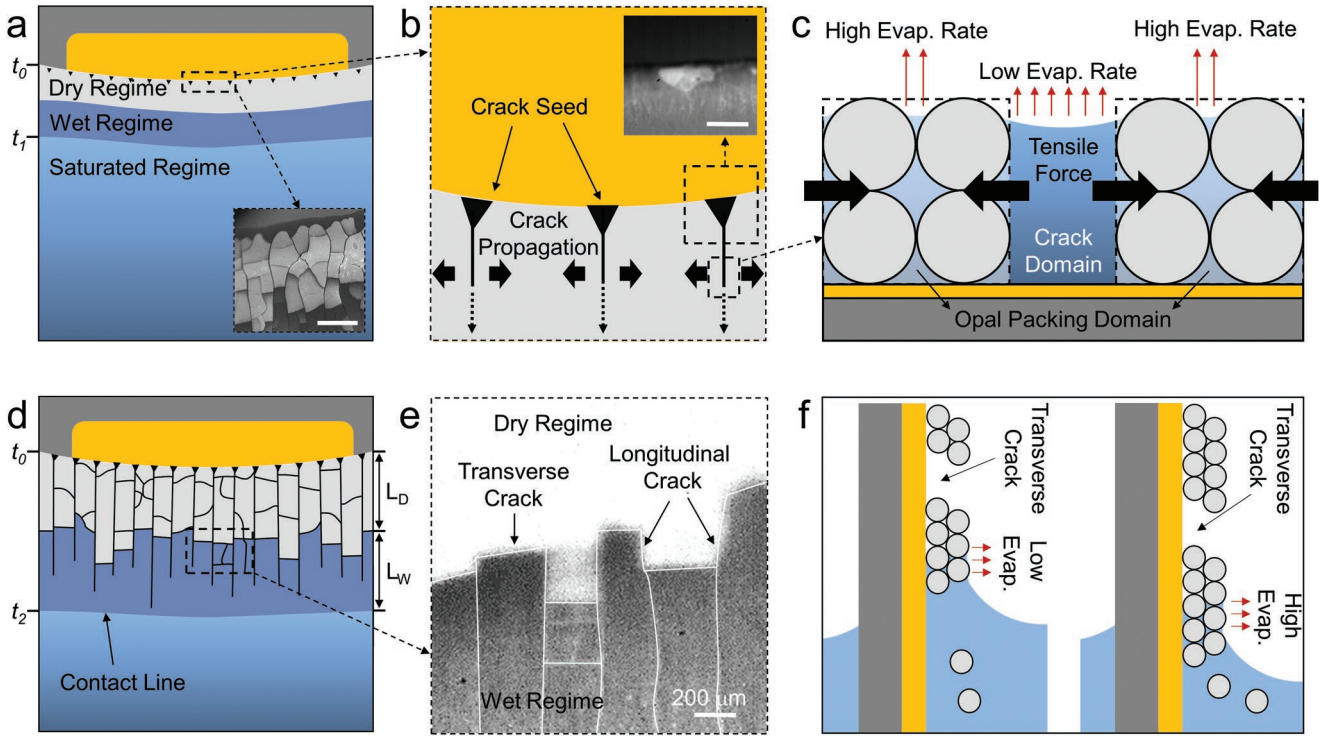

Figure 2. Crack formation and propagation mechanisms during the self-assembly. a) Three regimes during self-assembly process via vertical deposition method: the dry regime, the wet regime, and the saturated regime. The inset shows an SEM image of the top regime of a self-assembled opal film and has a scale bar of 500 µm. b) Crack seeds initiate at the top of the structure and are promoted in the dry regime. The inset shows a representative image of an initial crack seed. The inset scale bar is 200 µm. c) The liquid–vapor interline with smaller meniscus area (i.e., between packed spheres) leads to higher evaporation rates than that at the microcracks. The differences in evaporation rates generate tensile forces that facilitate longitudinal crack propagation. d,e) Longitudinal cracks propagate into the wet regime, whereas transverse cracks appear only in the dry regime or near the interface of the wet and dry regimes. f) Transverse cracks develop as the structure experiences tensile forces along the longitudinal direction. The illustrations show the effect of different evaporation rates occurring at the film surface on the formation of transverse cracks. As higher evaporation rates are introduced to the system, more particles are driven to the growth area, and the colloidal liquid level drops at a faster rate, leading to larger grain sizes.

of crystalline packing quality through an image analysis technique that utilizes Voronoi diagrams, as shown in **Figure 3**a (see the Supporting Information S3.2 for detail).[22] To segment images using Voronoi diagrams, top view scanning electron microscope (SEM) images of opal packings are processed through MATLAB. In detail, the Voronoi diagram employs distance-based partitioning algorithms to divide the image of the opal packing into multiple regions (i.e., Voronoi cells) containing one seed. The identified cells are then converted from pixels to area, which is defined as measured Voronoi area A_m. Multiple randomly selected locations (within the area of interest in Figure S1a, Supporting Information) of the opal are observed under the SEM to eliminate biases in selecting specific packing regions.

The opal crystallinity is defined as the ratio of ideal Voronoi area A_i to the measured Voronoi area A_m, where the ideal Voronoi cells are formed in HCP structures as observed in previous studies.[27,30,54] Therefore, the Voronoi cell of an ideal crystalline structure contains regular hexagons that are arranged into an array with a radius r as illustrated in Figure 3a (Supporting Information), where r is assumed to be equivalent to the average particle diameter measured from the SEM images (**Table 1** and Figure S5). Since crystallinity is observed to be independent of colloidal concentration and heating temperature, we quantify the opal crystallinity for all our case studies with different sphere diameters in Figure 3b. The crystallinity improves from 63% to 102%, as the sphere diameter increases from 100 to 600 nm, suggesting that 600 nm particles possess more tightly packed arrangements.

In addition to the packing quality identification by comparing the ideal and measured areas, the Voronoi diagram provides visualized information regarding specific defect types and their locations through image partitioning (Figure 3a). The resulting Voronoi cell shapes might deviate from the ideal hexagonal cell shape due to different types of defects, such as impurities, vacancies, and misalignments (Figure S6, Supporting Information). This approach to characterize the opal packing provides valuable analytical data that can be used to study specific defect types of colloidal films.[37,55]

2.3. Grain Characteristics

To understand the effects of experimental parameters on grain characteristics, we examine the changes in grain shapes, sizes, and structural thickness by employing image analysis techniques. Normalized grain dimensions are defined by dividing measured values of the grain size by the actual sphere

© 2019 WILEY-VCH Verlag GmbH & Co. KGaA, Weinheim

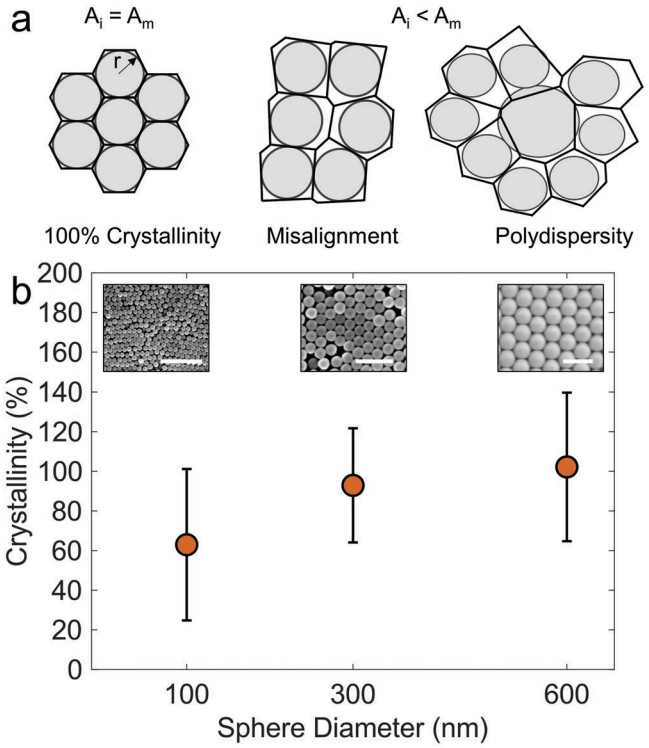

Figure 3. Crystallinity quantification using Voronoi diagram method. a) Illustrations show the ideal and actual Voronoi cells. The area of Voronoi cells with structural defects (i.e., misalignments) or particle defects (i.e., polydispersity) will be larger than that of the ideal Voronoi cell area A_i. b) The calculated crystallinity, the ratio of ideal area A_i to measured area A_m, is plotted for various sphere diameters, indicating that 600 nm particles form more ideal hexagonal packings. Error bars represent the standard deviation of A_m. Since the crystallinity is observed to be independent of colloidal concentration and heating temperature, the plot shows the representative values for all case studies discussed in this work. Insets show the detailed SEM images for various sphere diameters. The scale bar is 1 µm.

diameters provided in Table 1 and Figure S5 (Supporting Information) to quantify the sphere numbers constituting the measured values.

The grain shape's sensitivity to sphere diameter is investigated, revealing distinctive features, as shown in detailed micrographs in **Figure 4**a–c. The unique grain features are characterized by calculating the grain aspect ratio (i.e., grain height to width) and angular orientation (Figure 4d,e). While the average grain aspect ratios for all sphere diameters reside in a small range from 1–3 (Figure 4d), the grains themselves exhibit unique shapes, which can be further explained by introducing a grain orientation factor (Figure 4e). To measure the grain orientation factor, the grains are first identified through the delicate control of image thresholding. The angle φ (–90 °C < φ < 90 °C) between the *x*-axis and the major axis of each grain (Figure S7, Supporting Information) is then detected and converted to absolute values. The grain orientation factor is calculated by the following definition

$$\text{Grain orientation factor} = N(\varphi_{\text{vert}} + \varphi_{\text{hor}})/N(\varphi_{\text{tot}}) \quad (1)$$

where $N(\varphi_{\text{vert}})$ is the number of grains with the angles that are 85° < φ_{vert} < 90°, $N(\varphi_{\text{hor}})$ is the number of grains with the angles that are 0° < φ_{hor} < 5°, and $N(\varphi_{\text{tot}})$ is the total number of grains detected. Larger grain orientation factors are reported due to the more cubic-shaped grains produced by using smaller sphere diameters. For example, the orientation factor for the 100 nm spheres is 0.78, which means 78% of grains are orientated in vertical φ_{vert} or horizontal φ_{hor} angles. This might be attributed to weak interparticle adhesion forces, which can be explained by the reduction in crystallinity, failing to overcome directional tensile stresses that generates cracks. The 600 nm spheres exhibit a low orientation factor of 0.45, indicating that cubic grains are less frequent within the structure. Despite the low orientation factor, 600 nm spheres still exhibit longitudinal cracks, but show preferential hexagonal edges along rectangular-shaped grains.

We vary sub-micrometer sphere sizes to range from 100 to 600 nm to understand the effect of sphere diameters on the generated grain sizes. Relatively small sphere sizes are selected to evade undesirable deviations associated with large spheres (>2 µm) during the vertical deposition method such as poor packing quality due to gravitational effects on self-assembly or high polydispersity. Thus, for the selected sub-micrometer range, as the sphere diameter increases, the grains show a linear increase in height, width, and structural thickness (Figure S8a–c, Supporting Information), but a decrease in normalized sizes (Figure S8d–f, Supporting Information). This reduction in normalized grain sizes implies that using large sphere diameters results in lower number of spheres constituting the colloidal film.

While the sphere size affects grain characteristics, we further demonstrate that the colloidal concentration can also directly influence grain features. The colloidal solution concentration is varied from 0.6% to 2.0% and the self-assembly by-products are reexamined using the same procedures described above. Herein, increasing the colloidal concentration leads to the increases in grain height, width, and structural thickness, as plotted in **Figure 5**a–c. The normalized grain height, width, and structural thickness increase as well for the 100 and 300 nm sphere diameter cases (Figure S9, Supporting Information). However, as the sphere diameter increases from 300 to 600 nm, the normalized grain sizes display only subtle increases even at high (≈2%) concentrations. This can be explained by the competing roles between the interparticle adhesion forces and the gravitational forces in determining grain sizes during the vertical deposition self-assembly process. In other words, larger colloidal concentrations supply higher density of particles toward the growth regime located at the meniscus. This provides higher opportunities for spheres to assemble into structures and enables the structure to grow in all dimensions. However, for the relatively large 600 nm sphere diameter case, the gravitational force becomes a governing parameter, and the

Table 1. Measured sphere diameters.

Nominal sphere diameter [nm]	Measured sphere diameter [nm]	Standard deviation [nm]
100	109.2	11.4
300	282.9	24.2
600	578.3	27.8

© 2019 WILEY-VCH Verlag GmbH & Co. KGaA, Weinheim

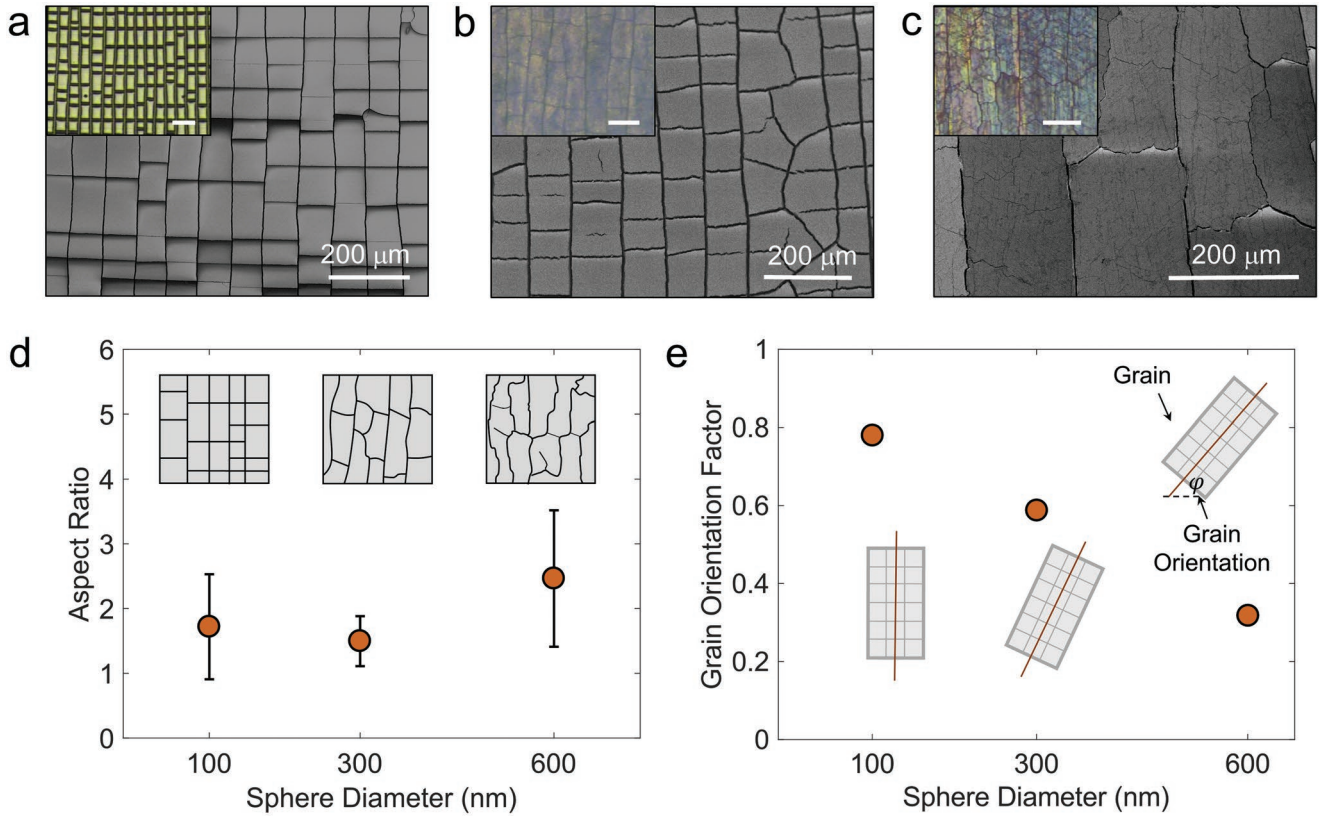

Figure 4. Grain shapes for varying sphere diameters. SEM images and optical microscope images (insets) of opals with a) 100, b) 300, and c) 600 nm sphere diameters show distinctive grain features. The inset scale bar is 200 μm. d) The aspect ratio of the grains is plotted for different sphere diameters. The insets illustrate the distinctive grain shapes. e) The grain orientation factor is plotted to characterize distinctive grain shapes. The decrease in the grain orientation factor with increasing sphere diameter confirms the decrease in the number of cubic-shaped grains. Inset illustrations describe how the grain orientation is defined.

influence of colloidal concentration of larger spheres on grain characteristics becomes less pronounced. Therefore, the grain characteristics are multidimensionally affected by the supply of sphere particles available due to the colloidal concentration.

Unlike the effect of sphere diameter and colloidal concentration on grain characteristics, the heating temperature can systematically control the growth of grain heights (Figure 5d–f). This study varies the heating temperatures from 43 to 93 °C to change the evaporation rates of the solvent and opal packing domain. The grain heights show small increases when temperatures are increased from 43 to 63 °C while the grain widths are observed to be relatively independent to all temperatures, as shown in Figure 5d. Once the heating temperature increases to 93 °C, the grains consisting of 300 and 600 nm spheres develop into single columns with heights exceeding ≈1 mm (Figure S10a,b, Supporting Information). The growth of these long column-like grains suggests an intensification in directional drying,[6,56,57] which might be attributed to the solvent evaporation rates at both bulk liquid and packing sphere level.

2.4. Grain Elongation Mechanisms

To explain the elongation of grains in high heating temperature conditions, we investigate the effect of evaporation rates of the solvent at the bulk liquid level and packing sphere level. This investigation discovers that high solvent evaporation rates reduce the frequency of transverse cracking by promoting efficient and expedient deposition of spheres. The evaporation rate of the solvent is highly dependent on the solvent surface temperature (instead of the heating temperature), which is directly measured using a thermocouple (Figure S10d, Supporting Information). As the heating temperatures of 43, 63, and 93 °C are tested, the solvent surface temperatures of 36, 42, and 65 °C are measured, respectively. The corresponding evaporation rate of the solvent is obtained by measuring the bulk meniscus location (Figure S10c, Supporting Information) with respect to time (Figure S10e,f, Supporting Information) for different heating temperatures. The average meniscus recession rate is ≈0.3, 0.4, and 1.0 μm s^{-1} for 43, 63, and 93 °C cases, respectively. A large meniscus recession rate implies that the liquid level drops at a high speed, allowing the quick deposition of spheres in the longitudinal drying direction which naturally reduces the chance for transverse cracks to form.

In addition to the investigation of bulk liquid evaporation, the high evaporation rates of the solvent at the packing sphere level effectively help grains grow in the longitudinal direction as well. As reported elsewhere,[58] the overall evaporation rates of a sessile drop (30 mm^3) increase up to ≈600% by changing heating temperatures from 25 to 70 °C.[58] By applying this

© 2019 WILEY-VCH Verlag GmbH & Co. KGaA, Weinheim

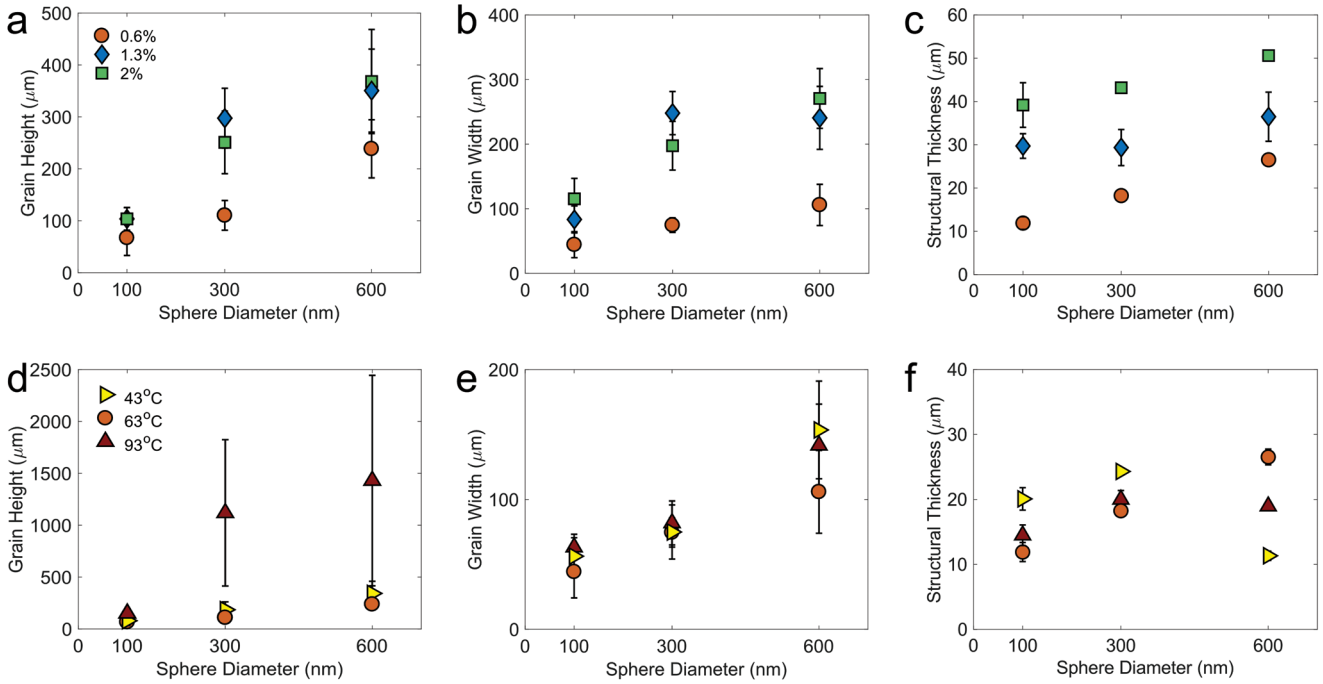

Figure 5. The effects of colloidal concentration and temperature on opal grain sizes and thickness. The grain height, width, and structural thickness are plotted a–c) for varying concentrations from 0.6% to 2% with a constant heating temperature of 63 °C and d–f) varying heating temperatures from 43 to 93 °C with a constant concentration of 0.6%. a–c) As the concentration increases, the grain sizes significantly increase in all aspects. d–f) The heating temperature mainly determines meniscus evaporation rates and governs grain heights rather than other parameters.

concept to the evaporation rate of the solvent at the packing sphere level, which has a comparable amount of liquid volume, the evaporation rates between sphere particles within the opal packing domain can be assumed to significantly increase with higher heating temperatures. The high evaporation rate occurring at the packing sphere level generates a large water flow, which allows spheres to deposit at a faster rate. This ultimately expedites colloidal deposition and growth, helping grains develop into elongated structures (Figure 2f). Therefore, the higher evaporation rates of the solvent at the bulk liquid level and packing sphere level promote efficient colloidal deposition in the drying direction, which ultimately results in the elongation of the grains.

2.5. Controllable Grain Characteristics

The thorough parametric studies presented strategies to harness uncontrollable defects developed during the self-assembly of colloidal spheres via the vertical deposition method. Furthermore, the combination of sphere diameter, colloidal concentration, and heating temperature contributes to the grain sizes and shapes (**Figure 6**). SEM images of the grains for different combinations of fabrication parameters are provided in Figures S11–S13 (Supporting Information). Throughout our investigation, grains develop into cubic structures with degraded crystallinity (≈60%), as sphere diameters decrease. The samples fabricated with larger spheres show larger grains than the samples fabricated with smaller spheres. Moreover, grain size can be grown in all dimensions by using higher colloidal concentrations. This type of grain growth is attributed to the dense supply of particles drawn toward the growth regime when a high concentration is used (Figure 5a–c). Finally, by increasing the heating temperature to 93 °C, the change in the evaporation rates of the solvent at the bulk liquid level and packing sphere level promotes grain elongation in the drying direction. The parametric results presented above will provide useful information such as grain and crack statistics to eventually allow us to fabricate crack-free structures. This might be demonstrated by using elastic substrates that can provide adequate contraction rates in the transverse direction after creating unidirectional (i.e., longitudinal) grains with the target substrate shrinkage of 3–10%.

3. Conclusions

In conclusion, we report the impact of fabrication parameters on the grain characteristics produced during colloidal self-assembly through the evaporative vertical deposition method with the aim to control structural patterns. The combination of sphere diameters, colloidal concentrations, and heating temperatures impacts the governing physical mechanisms such as evaporation phenomena associated with different drying regimes, thereby creating unique grain features. In particular, higher heating temperatures enable the creation of longitudinal grain features exceeding 1 mm, while larger spheres or higher colloidal concentrations lead to larger grain dimensions in all directions. To support the relationship between grain characteristics and packing quality, a new method using

© 2019 WILEY-VCH Verlag GmbH & Co. KGaA, Weinheim

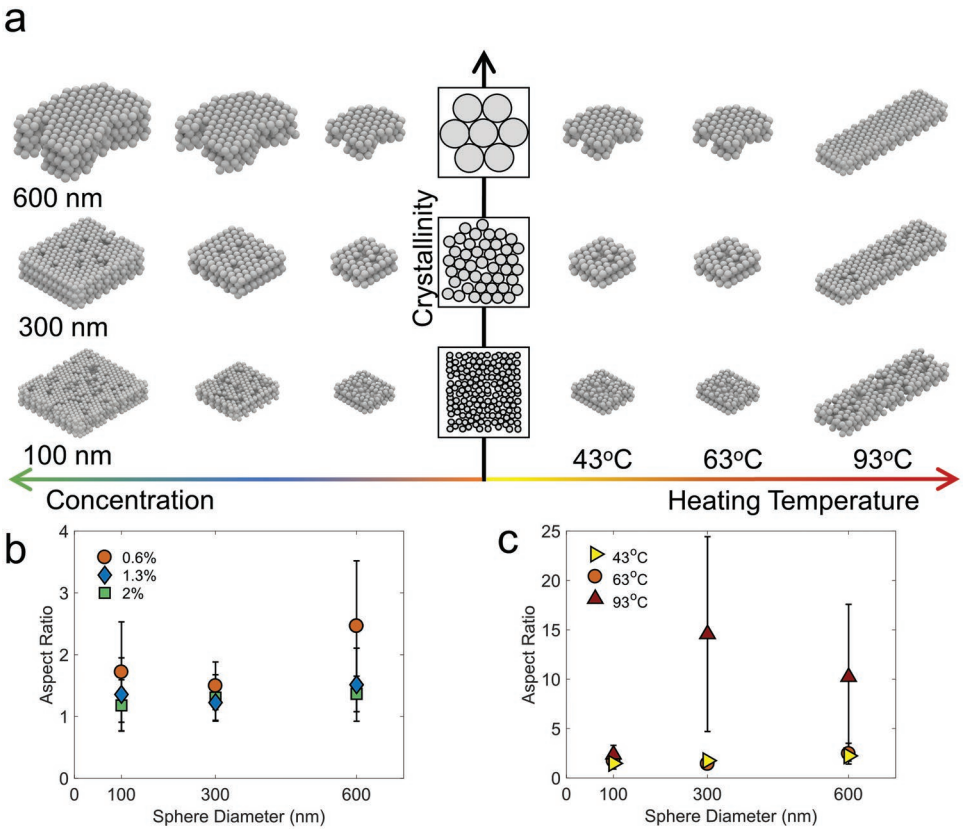

Figure 6. A regime map showing the effects of sphere crystallinity, colloidal concentration, and heating temperature on grain characteristics. a) As the sphere diameter increases, crystallinity improves, and the grain shapes change from cubic shapes to rectangular-shaped domains with hexagonal edges due to the level of crystallinity. Larger colloidal concentration supplies the growth regime a with greater number of spheres, and the grain dimensions correspondingly increase in all aspects. Higher temperatures increase the evaporation rates of the solvent at the bulk liquid level and packing sphere level, leading to the elongation of column-shaped grains. Grain aspect ratios for varying b) concentrations and c) heating temperatures are plotted.

Voronoi diagrams is employed to validate the colloidal crystal quality of the self-assembled opals while it simultaneously identifies specific defect types. Further work is needed to quantify stresses between grain domains with varying evaporation conditions during self-assembly. The fundamental understanding of fabrication parameters will provide significant insights into engineering novel nanopatterns with high periodicity as well as developing crack-free, large-scale crystalline structures by using self-assembly.

4. Experimental Section

Fabrication of Opals with Vertical Deposition Method: Crystalline opal structures were fabricated by employing the vertical deposition method.[11,15] Monodisperse sulfate latex beads with a concentration of 8% (Thermofisher Scientific, Life Technologies Corporation) were diluted in deionized water to 0.6%, 1.3%, and 2%. The particle distributions of 100–600 nm spheres diameters were measured using SEM images and are shown in Table 1 and Figure S5 (Supporting Information). Silicon substrates were evaporated with a 20 and 80 nm layer of titanium and gold, respectively, using a patterned shadow mask. The gold surface was chemically functionalized in 1×10^{-3} M aqueous sodium 3-mercapto-1-propanesulfonate for 24 h to render the surface hydrophilic, before rinsing it with deionized water, and drying it with compressed air. The prepared substrates were immersed in a colloidal solution. Heat was applied at the bottom of the well using a hot plate at a constant temperature reading of 43–93 °C. Self-assembly was carried out at room temperature with relative humidity of 55%, confirmed with a hygrometer (HI 9565, Hanna Instruments).

Image Processing: The samples were quantified and analyzed from SEM images (Magellan 400 XHR SEM, FEI). In this study, specific areas of interest known as the middle regime (Figure S1, Supporting Information) that are unaffected by precursory thickness development stages or concentration deviations were analyzed. The microcrack formation was monitored in real time with a high-speed camera (FASTCAM Mini AX, Photron) at 2000 fps. The camera observes the receding liquid meniscus where self-assembly occurs at a tilted angle of ≈30°.

Computational Fluid Dynamics: Evaporation rates of both opal packing domain and the crack domain were measured using computational fluid dynamics to support the observations of crack propagation and grain development. A model based on the geometry of packed spheres was designed (Supporting Information S2). The volume of fluid method was employed to calculate the time-dependent vapor-liquid phase change at the meniscus. Gravitational forces were neglected by selecting sphere diameters within the microscale range (from 0.1 to 100 µm). The unit cell was given a fluid feed to sustain evaporation by providing a velocity inlet boundary condition from the base of the unit cell. Heat was assumed to be transferred to the fluid via 1D conduction from the gold layer, as illustrated in Figure 1a. Under this assumption, a constant temperature $T_{bot} = 375.15$ K was applied at the base, $y = 0$, of the unit cell. A pressure outlet boundary condition of $p = 101.325$ Pa was applied at the top surface.

© 2019 WILEY-VCH Verlag GmbH & Co. KGaA, Weinheim

Supporting Information

Supporting Information is available from the Wiley Online Library or from the author.

Acknowledgements

This work was sponsored by the National Science Foundation (NSF) (Grant No. CBET-TTP 1752147, Dr. Jose Lage, the Program Director, Thermal Transport Processes). Y.S. is thankful for the financial support from the UC Irvine Mechanical and Aerospace Engineering Department Graduate Fellowship. The characterization was performed at the Irvine Materials Research Institute at UC Irvine.

Conflict of Interest

The authors declare no conflict of interest.

Keywords

colloidal crystals, cracking physics, crystalline defects, self-assembly, vertical deposition method

Received: October 29, 2018
Revised: December 29, 2018
Published online:

[1] N. Vogel, M. Retsch, C. A. Fustin, A. Del Campo, U. Jonas, *Chem. Rev.* **2015**, *115*, 6265.
[2] H. Cong, B. Yu, J. Tang, Z. Li, X. Liu, *Chem. Soc. Rev.* **2013**, *42*, 7774.
[3] W. Xu, Z. Li, Y. Yin, *Small* **2018**, *14*, 1801083.
[4] S. Ni, J. Leemann, H. Wolf, L. Isa, *Faraday Discuss.* **2015**, *181*, 225.
[5] D. J. Norris, E. G. Arlinghaus, L. Meng, R. Heiny, L. E. Scriven, *Adv. Mater.* **2004**, *16*, 1393.
[6] A. Hartsuiker, W. L. Vos, *Langmuir* **2008**, *24*, 4670.
[7] G. M. Whitesides, B. Grzybowski, *Science* **2002**, *295*, 2418.
[8] P. Jiang, M. J. McFarland, *J. Am. Chem. Soc.* **2004**, *126*, 13778.
[9] G. Roberts, *Langmuir-Blodgett Films*, Springer Science & Business Media, New York, USA **2013**.
[10] J. Shao, Y. Zhang, G. Fu, L. Zhou, Q. Fan, *J. Text. Inst.* **2014**, *105*, 938.
[11] G. Liu, L. Zhou, Y. Wu, C. Wang, Q. Fan, J. Shao, *J. Appl. Polym. Sci.* **2015**, *132*, 1.
[12] Z. Zhou, X. S. Zhao, *Langmuir* **2005**, *21*, 4717.
[13] Y. H. Ye, F. LeBlanc, A. Haché, V. Van Truong, *Appl. Phys. Lett.* **2001**, *78*, 52.
[14] W. L. Ash, M. R. Zlomislic, E. O. Oloo, D. P. Tieleman, *Biochim. Biophys. Acta, Biomembr.* **2004**, *1666*, 158.
[15] K. J. Edler, S. J. Roser, *Int. Rev. Phys. Chem.* **2001**, *20*, 387.
[16] B. Hatton, L. Mishchenko, S. Davis, K. H. Sandhage, J. Aizenberg, *Proc. Natl. Acad. Sci. USA* **2010**, *107*, 10354.
[17] M. A. McLachlan, D. W. McComb, *J. Mater. Chem.* **2004**, *14*, 2.
[18] G. Q. Liu, Z. S. Wang, Y. H. Ji, *Thin Solid Films* **2010**, *518*, 5083.
[19] H. Fudouzi, *J. Colloid Interface Sci.* **2004**, *275*, 277.
[20] M. S. Tirumkudulu, W. B. Russel, *Langmuir* **2005**, *21*, 4938.
[21] N. V. Dziomkina, M. A. Hempenius, G. J. Vancso, *Polymer* **2009**, *50*, 5713.
[22] S. N. C. Atsuyuki Okabe, B. Boots, K. Sugihara, *Spatial Tessellations: Concepts and Applications of Voronoi Diagrams*, Wiley & Sons, New York, USA **2009**.
[23] Y. A. Vlasov, V. N. Astratov, A. V. Baryshev, A. A. Kaplyanskii, O. Z. Karimov, M. F. Limonov, *Phys. Rev. E: Stat. Phys., Plasmas, Fluids, Relat. Interdiscip. Top.* **2000**, *61*, 5784.
[24] M. Curti, J. Schneider, D. W. Bahnemann, C. B. Mendive, *J. Phys. Chem. Lett.* **2015**, *6*, 3903.
[25] S. Wong, V. Kitaev, G. A. Ozin, *J. Am. Chem. Soc.* **2003**, *125*, 15589.
[26] A. S. Dimitrov, K. Nagayama, *Langmuir* **1996**, *12*, 1303.
[27] L. K. Teh, N. K. Tan, C. C. Wong, S. Li, *Appl. Phys. A* **2005**, *81*, 1399.
[28] S. C. Glotzer, M. J. Solomon, N. A. Kotov, *AIChE J.* **2004**, *50*, 2978.
[29] L. V. Woodcock, *Nature* **1997**, *385*, 141.
[30] P. Jiang, J. F. Bertone, K. S. Hwang, V. L. Colvin, *Chem. Mater.* **1999**, *11*, 2132.
[31] P. Born, S. Blum, A. Munoz, T. Kraus, *Langmuir* **2011**, *27*, 8621.
[32] Z. Cai, J. Teng, D. Xia, X. S. Zhao, *J. Phys. Chem. C* **2011**, *115*, 9970.
[33] L. Wang, X. S. Zhao, *J. Phys. Chem. C* **2007**, *111*, 8538.
[34] R. Chiu, T. Garino, M. Cima, *J. Am. Ceram. Soc.* **1993**, *76*, 2257.
[35] Z. Z. Gu, A. Fujishima, O. Sato, *Chem. Mater.* **2002**, *14*, 760.
[36] Y. Mino, S. Watanabe, M. T. Miyahara, *ACS Appl. Mater. Interfaces* **2012**, *4*, 3184.
[37] Y. Heo, S. Y. Lee, J. W. Kim, T. Y. Jeon, S. H. Kim, *ACS Appl. Mater. Interfaces* **2017**, *9*, 43098.
[38] C. Ding, J. C. Hu, W. Yuan, D. Z. Du, Y. Yang, G. Chen, K. Q. Zhang, *RSC Adv.* **2016**, *6*, 54976.
[39] B. P. Jiang, G. N. Ostojic, R. Narat, D. M. Mittleman, V. L. Colvin, *Adv. Mater.* **2001**, *13*, 389.
[40] Q. Yan, L. K. Teh, Q. Shao, C. C. Wong, Y. M. Chiang, *Langmuir* **2008**, *24*, 1796.
[41] Z. Cai, Y. J. Liu, J. Teng, X. Lu, *ACS Appl. Mater. Interfaces* **2012**, *4*, 5562.
[42] R. Ranjan, J. Y. Murthy, S. V. Garimella, U. Vadakkan, *Int. J. Heat Mass Transfer* **2011**, *54*, 153.
[43] T. J. Dusseault, J. Gires, M. T. Barako, Y. Won, D. D. Agonafer, M. Asheghi, J. G. Santiago, K. E. Goodson, *IEEE Intersoc. Conf. Therm. Thermomech. Phenom. Electron. Syst., 12th* **2014**, pp. 750–755.
[44] R. Ranjan, J. Y. Murthy, S. V. Garimella, *J. Heat Transfer* **2009**, *131*, 101001.
[45] T. J. Dusseault, J. G. Santiago, *Proc. ASME Int. Tech. Conf. Exhib. Packag. Integ. Electron. Photonic Microsys.* **2015**, pp. V002T06A004–V002T06A004.
[46] Q. N. Pham, M. T. Barako, J. Tice, Y. Won, *Sci. Rep.* **2017**, *7*, 10465.
[47] N. A. Kotov, Y. Liu, S. Wang, C. Cumming, M. Eghtedari, G. Vargas, M. Motamedi, J. Nichols, J. Cortiella, *Langmuir* **2004**, *20*, 7887.
[48] K. Y. Lee, J. Chun, J. H. Lee, K. N. Kim, N. R. Kang, J. Y. Kim, M. H. Kim, K. S. Shin, M. K. Gupta, J. M. Baik, S. W. Kim, *Adv. Mater.* **2014**, *26*, 5037.
[49] J. Lee, S. Shanbhag, N. A. Kotov, *J. Mater. Chem.* **2006**, *16*, 3558.
[50] Y. Zhang, S. Wang, M. Eghtedari, M. Motamedi, N. A. Kotov, *Adv. Funct. Mater.* **2005**, *15*, 725.
[51] T. Gillespie, W. J. Settineri, *J. Colloid Interface Sci.* **1967**, *24*, 199.
[52] Y. G. Ko, D. H. Shin, *J. Phys. Chem. B* **2007**, *111*, 1545.
[53] B. Griesebock, M. Egen, R. Zentel, *Chem. Mater.* **2002**, *14*, 4023.
[54] K. Montazeri, H. Lee, Y. Won, *Int. J. Heat Mass Transfer* **2018**, *122*, 59.
[55] P. Massé, S. Reculusa, K. Clays, S. Ravaine, *Chem. Phys. Lett.* **2006**, *422*, 251.
[56] K. A. Shorlin, J. R. De Bruyn, M. Graham, S. W. Morris, *Phys. Rev. E: Stat. Phys., Plasmas, Fluids, Relat. Interdiscip. Top.* **2000**, *61*, 6950.
[57] L. Pauchard, M. Adda-Bedia, C. Allain, Y. Couder, *Phys. Rev. E: Stat. Phys., Plasmas, Fluids, Relat. Interdiscip. Top.* **2003**, *67*, 4.
[58] M. Ait Saada, S. Chikh, L. Tadrist, *Phys. Fluids* **2010**, *22*, 112115.

© 2019 WILEY-VCH Verlag GmbH & Co. KGaA, Weinheim